Science of the Total Environment 994 (2025) 180041

Contents lists available at ScienceDirect

Science of the Total Environment

journal homepage: www.elsevier.com/locate/scitotenv

Deep learning based aerosol particle classification for the detection of ship emissions

Guanzhong Wang [a], Heinrich Ruser [a,*], Julian Schade [b], Seongho Jeong [b], Johannes Passig [c,d], Ralf Zimmermann [c,d], Günther Dollinger [a], Thomas Adam [b,d]

[a] Institute for Applied Physics and Measurement Technology, University of the Bundeswehr Munich, 85577 Neubiberg, Germany
[b] Institute of Chemistry and Environmental Engineering, University of the Bundeswehr Munich, 85577 Neubiberg, Germany
[c] Institute of Chemistry, Division of Analytical and Technical Chemistry, University of Rostock, 18059 Rostock, Germany
[d] Joint Mass Spectrometry Center (JMSC), Helmholtz Zentrum München, Neuherberg 85764, Germany

HIGHLIGHTS

- Chemical composition of individual aerosol particles using single-particle mass spectrometry (SPMS)
- Deep learning for the classification of spectral data to identify the pollution sources of aerosol particles
- SPMS, deep learning, meteorological conditions and Automatic Identification System (AIS) for ship emissions detection

GRAPHICAL ABSTRACT

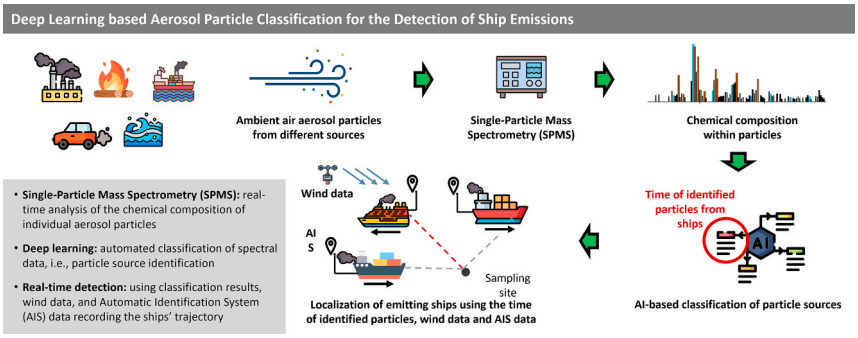

ARTICLE INFO

Editor: Ouyang Wei

Keywords:
Aerosol particles
Deep learning
Environmental monitoring
Ship emission detection
Single-particle mass spectrometry

ABSTRACT

Increasing recognition of the impact of shipping on air pollution has led the International Maritime Organization (IMO) to establish Sulfur Emission Control Areas (SECA) to reduce emissions. Within SECA, ships must switch to low-sulfur fuel or use a scrubber technique to clean their exhaust gases. Conventional monitoring methods are limited by detection range, real-time data availability, and challenges in source attribution. This study describes a monitoring system that combines single-particle mass spectrometry (SPMS) with deep learning to overcome these shortcomings. SPMS can reveal the chemical composition of individual airborne aerosol particles, with the capability to detect emissions over several kilometers, enabling real-time pollution source identification. To automatically process the complex mass spectral data, a convolutional neural network (CNN) was designed, achieving 92 % accuracy in classifying 13 distinct classes of abundant aerosol particles. The results demonstrate that the proposed detection system enables to automatically classify aerosol particles from multiple sources. Of particular concern in this study is the in-situ analysis of particles from ship exhaust plumes, to rapidly identify ships running on polluting heavy fuel oil. Focusing on unique particles containing vanadium ($^{51}V^{+}/^{67}[VO]^{+}$), nickel ($^{58/60}Ni^{+}$), and iron ($^{54/56}Fe^{+}$) ions, designated as V-rich class, the real-time classification makes it possible to reliably detect particles from heavy fuel oil (HFO) combustion. In addition, to locate the emission

* Corresponding author.
E-mail address: heinrich.ruser@unibw.de (H. Ruser).

https://doi.org/10.1016/j.scitotenv.2025.180041
Received 16 April 2025; Received in revised form 2 July 2025; Accepted 3 July 2025
Available online 10 July 2025

sources, the CNN's predictions are linked to local wind measurements and ship trajectories provided by the Automatic Identification System (AIS). During a one-week monitoring period, 21 ships passing the measurement site 80 times in distances of up to ~1.3 km were detected using HFO.

1. Introduction

Ships play a fundamental role in the global transportation of goods. Statistics from the United Nations Conference on Trade and Development show that >80 % of the world's trade was transported by sea (UNCTAD, 2018), with an expected rise by a further 3.2 % in 2024 (UNCTAD, 2023). Cargo ships as well as ferries, cruise liners and other passenger ships as the main mean of maritime transportation have become a huge and growing source of carbon dioxide (CO_2), nitrogen oxides (NO_x), sulfur oxides (SO_x), and particulate matter (PM) in the atmosphere (Eyring et al., 2010; Toscano and Murena, 2019; Zhu et al., 2018), which apart from contributing to global warming intensify air pollution in coastal areas, potentially causing human's respiratory problems leading to premature death (Blasco et al., 2014; Fuglestvedt et al., 2009; Viana et al., 2014).

In order to reduce these harmful effects of ship emissions, the International Maritime Organization (IMO) established Sulfur Emission Control Areas (SECA) to mitigate and control environmental pollution caused by ship exhaust. SECA include, for example, most of North American coast regions, and the North Sea and the Baltic Sea in Europe. More areas are under discussion for becoming SECA (Cariou et al., 2024; Dulebenets, 2016; Lähteenmäki-Uutela et al., 2019).

In compliance with the emission standards established by the IMO, in SECA ship must run on low-sulfur fuels with a sulfur content of no more than 0.1 % m/m (mass by mass) (Dulebenets, 2016; IMO, 2016), such as marine gas oil (MGO). Alternatively, ships upgraded with fuel aftertreatment systems including sulfur scrubbers are allowed to continue to use high-sulfur fuels (1…2.5 % m/m (Jeong et al., 2023)), such as heavy fuel oil (HFO), in SECA (Cariou et al., 2024; Lähteenmäki-Uutela et al., 2019). Many ships still run on cheaper high-sulfur fuels with scrubbers within SECA (Abdul Jameel et al., 2019; Zis et al., 2022). Most scrubbers, however, utilize seawater for purification and discharge the mixture into the sea, causing additional environmental and biological problems (Eyring et al., 2010; Ni et al., 2020; Zhou and Wang, 2020). Hence, there is an immediate need for effective measures to detect the emissions from ships in compliance with the IMO standards.

Most of the currently established detection systems for monitoring ship emissions use gas-phase measurement instruments (Kattner et al., 2015; Toscano and Murena, 2019; Zhou et al., 2022a). These systems are typically deployed near coastlines or in port areas to measure the change of gas concentrations, such as CO_2, SO_x, and NO_x, during the passage of ships. Gas-phase measurements are significantly affected by the distance between the emission source and the measurement station, with an effective measuring range of only a few hundred meters due to the rapid dilution of the gas as it spreads. Ship-based monitoring (Beecken et al., 2015; Fu et al., 2013; Zhou et al., 2022a) involves the installation of instruments on-board to measure the emissions. Although this way of monitoring is sensitive, it is also costly and inefficient, since only one ship at a time can be inspected. Airborne monitoring systems installed on manned or unmanned aircraft (Mellqvist et al., 2017; Villa et al., 2019; Yuan et al., 2020) are not suitable for permanent monitoring.

As aerosol particles can keep parts of their source-specific chemical composition even after long air transport, particle-phase measurement instruments are an effective approach to extend the detection range of air quality monitoring (Dall'Osto and Harrison, 2006; Passig et al., 2021). Single-particle mass spectrometry (SPMS) is a real-time measurement technique that reveals the chemical composition of individual particles on behalf of their mass spectra, with high measurement rates of up to hundreds of particles per minute (Passig and Zimmermann, 2021; Pratt and Prather, 2012; Schade et al., 2019). For automatic analysis of this amount of data, machine learning approaches for fast and efficient pattern recognition are being sought (Beck et al., 2024; Christopoulos et al., 2018; Wan et al., 2024; Wang et al., 2024a). Accurate classification of a large variety of MS patterns offers new ways for air pollution monitoring and source apportionment, to locate pollution sources and the amount they contribute to ambient air pollution levels (Dall'Osto and Harrison, 2006; Heikkilä et al., 2024; Shen et al., 2024; Su et al., 2024), as well as ship emissions (Passig et al., 2022, 2021; Zhou et al., 2022b), traffic emissions (Toner et al., 2006; Xu et al., 2024), industrial pollutions (Arndt et al., 2021; Ye et al., 2025), etc.

This paper describes a real-time application for in-site analysis and identification of emission sources of individual airborne particles in the atmosphere using SPMS and deep learning, in particular based upon a convolutional neural network (CNN). We focus on analyzing particles from ship emissions, transported by wind to a land-based measurement site, specifically on particles within the predictions signaling the combustion of polluting HFO. In order to identify and locate ships running on HFO, (1) CNN's classification, (2) wind data (direction and speed) from a local metrological station and, (3) entries in the Automatic Identification System (AIS) recording the trajectory of ships are integrated for the first time. Fig. 1 shows the flowchart of the monitoring system.

In Section 2, the SPMS measurement device is briefly described and typical MS patterns in different classes of abundant airborne particles are presented. In Section 3, several conventional approaches of mainly expert-assisted, off-line MS patterns analysis are discussed and the new classification method based on deep learning is introduced. In Section 4, it is described how the data obtained from a month-long measurement campaign are used to create a benchmark dataset to train, validate, and test a CNN model to provide accurate and efficient identification of the chemical signature of aerosol particles. In Section 5, results are given and discussed, showing that the new system is a powerful tool to realize remote and real-time air quality monitoring and is particularly suitable for the detection of ship emissions in coastal areas.

2. Single-particle mass spectrometry

SPMS is a highly sensitive real-time technique for profiling the chemical signatures of individual airborne aerosol particles. The operating principles and parameters of SPMS have been described in detail in other studies (Passig and Zimmermann, 2021; Pratt and Prather, 2012; Schade et al., 2019). In short, the entering particles are isolated using an aerodynamic lens (Part I in Fig. 2(a)), then sized via light scattering with a setup that includes a pair of continuous-wave lasers (wavelength 532 nm), ellipsoidal mirrors, and photomultipliers (Part II). The individual particles are then exposed to a triggered UV laser pulse (KrF-excimer laser, wavelength 248 nm) for laser desorption/ionization (LDI), and the ionized anions and cations are separated and detected in two time-of-flight (TOF) mass spectrometers (Part III). The resulting bipolar mass spectrum reveals the chemical composition of a single particle by displaying the intensity distribution of mass-to-charge ratios (m/z) for the anions and cations, see an example in Fig. 2(b). By examining specific combinations of peaks in the MS patterns, the probable emission source of the particles can be determined.

Fig. 3 shows several representative examples of chemical signatures of particles from different sources. The preprocessed and discretized ($\Delta m/z = 1$) MS pattern for each particle contains signal intensities in the range of the mass-to-charge ratio (m/z) from −120 to +120 and is normalized by the maximum intensity of the positive and negative mass spectra, respectively.

Fresh particles from traffic emissions have dense elemental carbon (EC) ion signals $^{12n}C_n^{\pm}$ (Dall'Osto and Harrison, 2006; Healy et al., 2010), as shown in Fig. 3(a); biomass combustion is known to produce particles containing EC and organic carbon (OC) (Dall'Osto and Harrison, 2012; Toner et al., 2006), see Fig. 3(b); calcium and its related ions (Fig. 3(c)) stem mainly from engine lubricant additives (Moffet et al., 2008; Passig et al., 2021); particles with strong iron signals but small sulfate signatures (Fig. 3(d)) are associated with the combustion of low-sulfur fuels such as MGO (Passig et al., 2022; Wang et al., 2019); the combination of the transition metal ions vanadium ($^{51}V^+/^{67}[VO]^+$), nickel ($^{58/60}Ni^+$), and iron ($^{54/56}Fe^+$) (Fig. 3(e)) is characteristic for the combustion of HFO fuel used for marine engines (Ault et al., 2009; Passig et al., 2021); sea salt particles from sea spray as in Fig. 3(f) have ions associated with sodium and chlorine (Köllner et al., 2017; Shen et al., 2019).

3. SPMS data classification

For every detected airborne aerosol particle, SPMS generates an MS pattern representing the chemical composition of that particle. For plumes of high density of particles, tens of particles are detected per second. For fast inspection of a vast amount of MS patterns, ion marker screening based on preset mass numbers or the ratios between specific ion peak intensities is often used (Rosewig et al., 2024). Many mass numbers, however, have multiple meanings depending on the type of emission source, which makes the screening inaccurate. For example, regarding the mass numbers used to determine V-rich particles, m/z 51 could be $^{51}V^+$ or $^{51}[C_4H_3]^+$, 56 could be $^{56}Fe^+$; or $^{56}[CaO]^+$, 60 could be $^{60}Ni^+$or $^{60}C_5^+$, and 67 could be $^{67}[VO]^+$or $^{67}Zn^+$. Moreover, identification based on ratios of ion peak intensities is applicable only to stable ratios. For our application, this is often not the case, see Fig. 4.

Therefore, for classification of MS patterns, unsupervised clustering algorithms such as K-means and ART-2a are most used in the field. Unsupervised clustering does not require training and allows new spectral features to be discovered during expert-assisted post-processing. In order to bring down the usually large number of clusters proposed by the unsupervised clustering algorithms to the number of intended classes, clusters are merged in a multi-step expert-assisted off-line process (Chen et al., 2024; Dall'Osto and Harrison, 2006, 2012; Passig et al., 2022, 2021). Clearly, unsupervised clustering makes it difficult to obtain accurate, stable and continuous outputs and manual post-processing prevents the aerosol particles analyzed in-situ to be classified in real-time.

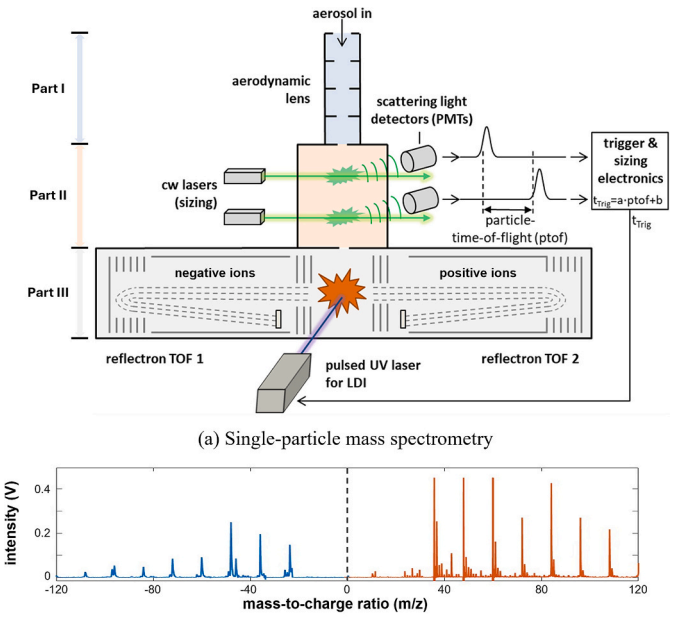

(a) Single-particle mass spectrometry

(b) Exemplary negative and positive mass spectra generated by SPMS

Fig. 2. (a) Configuration of the SPMS instrument (Passig and Zimmermann, 2021) consisting of three main parts: aerodynamic lens (Part I), sizing unit (velocimetry laser system) (Part II), laser desorption/ionization (LDI) and bipolar TOF mass spectrometer (Part III). (b) Typical generated mass spectral pattern.

In a few studies (Christopoulos et al., 2018; Wan et al., 2024; Wang et al., 2024a), supervised machine learning methods such as Random Forest, Support Vector Machines, and Multi-layer Perceptron were proposed for the classification of MS patterns. Based on labeled data, predictive models are trained to classify huge amounts of data in a fully automated way.

In contrast to traditional machine learning approaches, deep

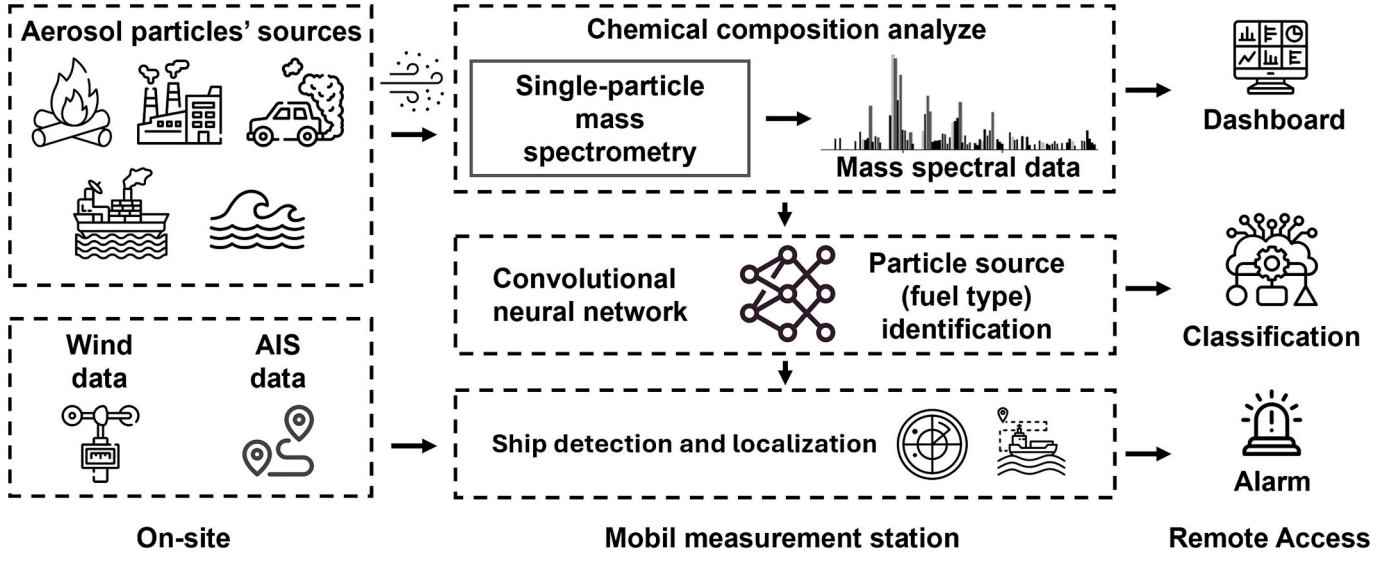

Fig. 1. Flowchart of the monitoring system for ship emission detection based on profiling air-transported aerosol particles by a land-based single-particle mass spectrometry (SPMS). The resulting mass spectra are classified in real-time by deep learning (realized as a convolution neural network, CNN). In order to localize emission sources, predictions of relevant classes are linked to local wind measurements (direction and speed) and reported position data (AIS) of individual ships. (Icons are provided by flaticon.com).

learning-based architectures such as convolutional neural networks (CNNs) perform adaptive feature extraction, making them well-suited for processing complex data. CNNs are free from the dependence on expert-engineered learning features and have been successfully applied to a large variety of input data such as text, image, and audio (LeCun et al., 2015). The specific CNN architecture, which is built upon convolution layers, allows the weights of its filters (called convolutional kernels) to be continuously adjusted and optimized during training. This enables the network to automatically generate characteristics of feature maps that capture important patterns from the input data. The performance of such high-dimensional abstract features learned by convolution operations has been shown to outperform the hand-designed learning features (Alzubaidi et al., 2021; LeCun et al., 2015).

To extract the learning features from the one-dimensional (1D) SPMS data for classification, 1D-CNN architectures were designed (Wang et al., 2023; Xu et al., 2024). The resulting small convolutional kernels with dimensions 3×1 (Wang et al., 2023), however, make it difficult to capture both local and global features simultaneously, potentially losing relationships between 'distant' parts of a MS vector on the mass axis. Increasing the size of convolutional kernels in 1D-CNN did not improve the performance. Alternatively, through a serpentine layout the MS vector can be converted into a two-dimensional (2D) representation to be used as input to a 2D-CNN architecture. In a 2D representation the spectral information is stored in a compact format, enabling to efficiently extract different specific features of complex MS patterns (Wang et al., 2024b). In this study we use a 2D-CNN architecture to classify the MS data and compared the classification results among different architectures, see Section 5.1.

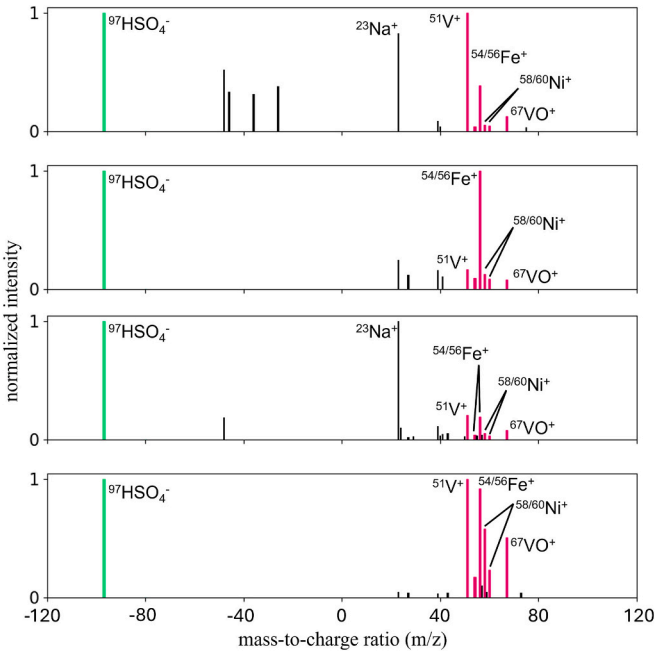

Fig. 4. Exemplary mass spectral patterns of four vanadium-containing aerosol particles (V-rich class) with different ratios of peak intensities of characteristic ion markers (in magenta).

4. Detection of ship emissions

4.1. Measurement campaign

The aim of this study is to investigate, how well the proposed deep learning-based classification of individual aerosol particles can be applied on-line to describe and localize emission sources of aerosol particles produced by the combustion of marine fuels from ships. Specifically, we focus on analyzing the emissions of ships entering and leaving the port of Rostock, Germany, situated on the south coast of the Western Baltic Sea, with the purpose to identify ships running on cheap but heavily polluting fuels like HFO. To the best of our knowledge, this is the first time that the SPMS technology is combined with deep learning technologies, local wind conditions and tracking data of registered ships (AIS) to classify emissions from fuel combustion of ships and localize its source.

The trade and ferry port of Rostock is the largest German Baltic Sea port with an annual cargo throughput of >30 Mt and a passenger volume of >2.5 million. The unique SPMS instrument, manufactured by Photonion GmbH, Germany, was installed in a trailer and moved to the entrance of the harbor area. The position of the measurement site (54°10′14.8″ N, 12°06′24.7″ E) was chosen to be close to the main channel connecting the port to the Baltic Sea, ~0.5 km east (often

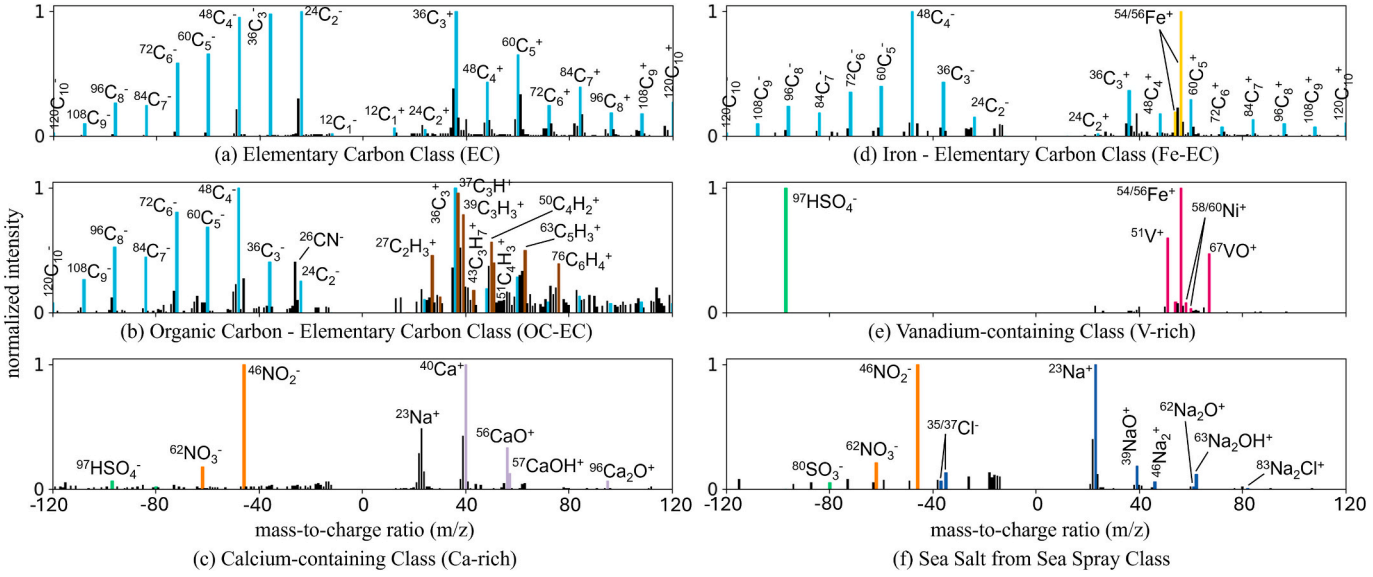

Fig. 3. Exemplary mass spectral patterns of aerosol particles of 6 of the 13 predefined classes. The mass-to-charge ratios (m/z) range from −120 to +120, and the intensities for negative and positive m/z are separately normalized by the maximum intensities of anions and cations. The colored ion peaks show characteristic class-specific markers for different particle classes.

downwind) of the channel and ~2 km north of the port, see Fig. 5. The city of Rostock (~200,000 inhabitants) is about 10 km to the south.

With westerly (northwest, west, southwest) winds, aerosol particles from the exhaust plume of ships in the maritime channel will be transported to the sampling site. The ambient air was sampled at a height of ~7 m above sea level. A concentrator (model 4240, MSP Corp., Shoreview, MN, USA) was used to concentrate the particles from a 300 L/min intake air stream into a 1 L/min carrier gas stream. The particles then passed through a dryer (model MD-700-12S-1, Perma Pure LLC, Lakewood, NJ, USA) and were concentrated again in a virtual impactor stage at the inlet of the SPMS right above the aerodynamic lens (Rosewig et al., 2023). According to the specifications of the concentrator and the SPMS, the analyzed single particles were in the size range of 0.25–2.5 μm.

In this study, data from a 34-day field measurement campaign conducted from July 1st to August 3rd 2022, were used. The wind data (direction and speed) at the time of the measurements are available online from the German Weather Service (DWD), Station 4271 (54°10′49.1″N, 12°04′50.9″E), located about 2 km northwest of the sampling site, see Fig. 5. The data from the meteorological station were recorded every 10 min (German Weather Service (DWD), 2022). From the wind direction and speed, the delay between the emission and the time of measurement at the sampling site can be deduced. To match the detected particles with a specific ship passing the maritime channel in the proper location and time, we used an AIS logger data recording the positions (latitude and longitude) over time (along with the ship's name, length, type, and other data) of all ships in the area.

In Fig. 5, the Search Area for ship detection is marked as a red transparent surface. All ships entering or leaving the harbor sail through the straight maritime channel (length ~3 km, width ~250 m) linking the harbor area with the Baltic Sea. As Search Area for our investigations, we chose a ~2 km long section of that maritime channel, with latitudes ranging from 54°09′42.1″N to 54°10′47.3″N, such that the latitude of the sampling site (54°10′14.8″N) marks the mean of the latitude range of the Search Area, with a distance of about 1 km from both its northern and southern boundaries and about 500 m to the main shipping lane at the closest point of passing.

With a reduced maximum allowed cruising speed of all vessels in the maritime channel, the average passage time through the Search Area is about 10 min.

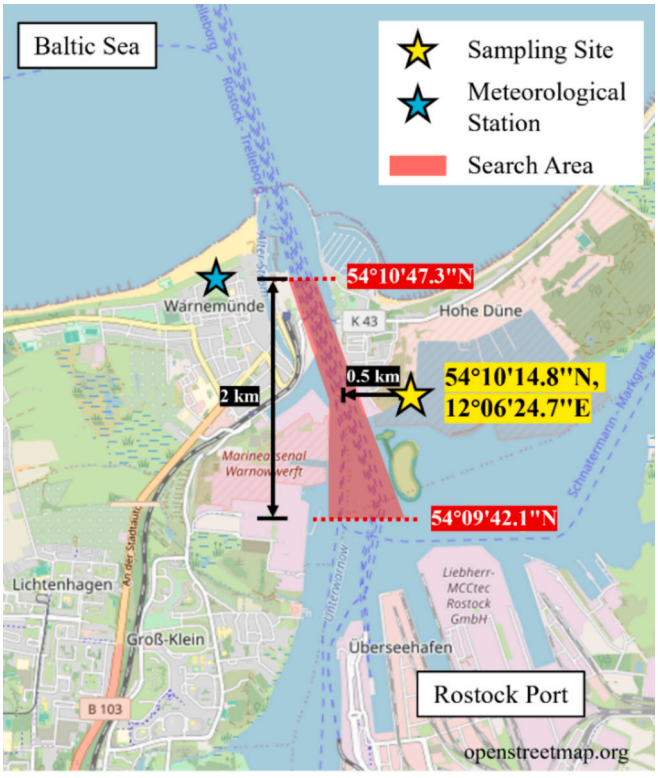

Fig. 5. Map of the Rostock harbor area. (Source: openstreetmap.org) The red transparent surface highlights the Search Area for ship detection, covering a 2-km-stretch of the maritime channel linking the city's port with the Baltic Sea. Also marked are the locations of the sampling site and the meteorological station. The closest distance from the sampling site to the shipping lane is approx. 500 m, and the distance to the port is also about 2 km.

4.2. Benchmark dataset

During the measurement campaign, the chemical composition of about 1.5 million individual aerosol particles was analyzed with the SPMS device at the sampling site. Of these, 37,406 particle MS patterns were selected and manually labeled to build a benchmark dataset for training and testing a 2D-CNN classification model. The dataset contains particles representing the 13 most abundant particle classes in the local ambient atmosphere during the period of the measurement campaign. The classes were defined based on expert knowledge on typical mass spectral patterns. In the off-line labeling process, each particle was attributed to one of those 13 predefined classes, analyzing occurring combinations of different chemical components (i.e. positions of peaks in the MS patterns) and their intensities. To reduce bias from subjectivity, the labeling process was assisted by multiple experts. In Table 1, the 13 classes are listed, associated with main emission sources, major ion markers used to identify characteristic chemical precursors of each class and the number of samples (particles) available in the benchmark dataset.

MS examples given in Fig. 3 embody the chosen guideline for labeling mass spectra of individual particles. Generally, the assignment to a class was based on the occurrence of dominating ion markers (see Table 1). In practice, the mass spectrum of many particles contained ions which are characteristic for more than one class. In those cases, the ion peak with the highest intensity was said to determine the class label of that particle. Notably, we allowed for one exception to this rule: Spectra showing any combination of ion peaks of vanadium ($^{51}V^{+}$/$^{67}[VO]^{+}$), nickel ($^{58/60}Ni^{+}$), and iron ($^{54/56}Fe^{+}$) of noticeable intensity, which is characteristic for HFO combustion, were labeled as belonging to the V-rich class, even if none of those ion peaks were dominant in the MS patterns. This 'sensitive' rule ensures that none of the relatively few vanadium-containing particles found in the measurement data is missed.

Since the concentration of aerosol particles in the atmosphere can greatly vary depending on the emission source, to create a balanced dataset containing patterns with roughly the same number for every class was difficult. The chosen sampling site was in close distance to a busy maritime channel within a SECA. Therefore, a significant number of particles from the combustion of low-sulfur MGO fuel (permitted in SECA) occurred in the atmosphere and hence in the benchmark database. Many iron-containing particles were detected due to the LDI laser wavelength of 248 nm, matching a strong absorption line of atomic iron (Passig et al., 2022). These particles were further grouped into subclasses (Fe-EC, Fe-Sul-Nit, Fe-Nit-EC, Fe-Nit, Fe-dominant), based on their degree of aging (a rough estimate of the distance to the emission source). Compared to particles from MGO combustion, there were fewer particles from HFO combustion (allowed in SECA only with a scrubber), and therefore these particles from HFO combustion (V-rich class) were not sub-grouped into additional classes.

5. Results and discussion

5.1. Classification of aerosol particles

The 2D-CNN architecture used in this study to train the model for the classification of MS patterns was successfully tested earlier (Wang et al.,

Table 1
Overview of the 13 particle classes in the labeled benchmark dataset. Prominent emission sources and the corresponding ion markers of particles are summarized from the literature and expert experience.

No.	Class	Prominent emission sources	Ion markers	No. of samples	%
1	Elemental carbon (EC)	Traffic emissions, biomass burning (Ault et al., 2009; Dall'Osto and Harrison, 2006; Healy et al., 2010; Toner et al., 2006)	EC: $^{12}C^{\pm}$, $^{24}C_2^{\pm}$, …, $^{120}C_{10}^{\pm}$	816	2.2
2	Organic and elemental carbon (OC-EC)	Biomass burning, traffic emissions (Dall'Osto and Harrison, 2006, 2012; Shen et al., 2019; Toner et al., 2006)	OC: $^{27}[C_2H_3]^+$, $^{37}[C_3H]^+$, $^{39}[C_3H_3]^+$, $^{43}[C_3H_7]^+$, $^{51}[C_4H_3]^+$, $^{63}[C_5H_3]^+$, etc.; EC	3383	9.0
3	K-rich	Biomass burning (Dall'Osto and Harrison, 2006; Healy et al., 2012, 2010; Moffet et al., 2008)	$^{39/41}K^+$	3300	8.8
4	Ca-rich	Lubricating oil of engines (Dall'Osto and Harrison, 2006; Moffet et al., 2008; Passig et al., 2021; Toner et al., 2006)	$^{40}Ca^+$, $^{56}[CaO]^+$, $^{57}[CaOH]^+$, $^{112}[CaO]_2^+$	3238	8.7
5	V-rich	HFO fuel emissions (Ault et al., 2009; Passig et al., 2022, 2021; Toner et al., 2006)	$^{51}V^+$, $^{67}[VO]^+$; $^{54/56}Fe^+$; $^{58/60}Ni^+$	943	2.5
6	Mn-rich	Industrial emissions (Arndt et al., 2021)	$^{55}Mn^+$	2904	7.8
7	Fe-EC	Low-sulfur fuel emissions (fresh) (Healy et al., 2009; Passig et al., 2022, 2021; Wang et al., 2019)	$^{54/56}Fe^+$, $^{73}[FeOH]^+$; EC	3306	8.8
8	Fe-Sul-Nit	Low-sulfur fuel emissions (moderately aged) (Healy et al., 2009; Passig et al., 2022, 2021; Wang et al., 2019)	$^{54/56}Fe^+$, $^{73}[FeOH]^+$; Sulfate: $^{80}[SO_3]^-$, $^{96}[SO_4]^-$, $^{97}[HSO_4]^-$; Nitrate: $^{46}[NO_2]^-$, $^{62}[NO_3]^-$	2992	8.0
9	Fe-Nit-EC	Low-sulfur fuel emissions (moderately aged) (Healy et al., 2009; Passig et al., 2022, 2021; Wang et al., 2019)	$^{54/56}Fe^+$, $^{73}[FeOH]^+$; Nitrate; EC	3451	9.2
10	Fe-Nit	Low-sulfur fuel emissions (aged) (Healy et al., 2009; Passig et al., 2022, 2021; Wang et al., 2019)	$^{54/56}Fe^+$, $^{73}[FeOH]^+$; Nitrate	3050	8.2
11	Fe-dominant	Low-sulfur fuel emissions (aged) (Healy et al., 2009; Passig et al., 2022, 2021; Wang et al., 2019)	$^{54/56}Fe^+$, $^{73}[FeOH]^+$; negative signals are empty or very weak	3423	9.2
12	Salt-Fe	Mixed state (Passig et al., 2022)	$^{54/56}Fe^+$, $^{73}[FeOH]^+$; Salt: $^{23}Na^{\pm}$, $^{39}[NaO]^+$, $^{62}[Na_2O]^+$, $^{63}[Na_2OH]^+$, $^{35/37}Cl^-$	3300	8.8
13	Sea spray	Sea salt (Dall'Osto and Harrison, 2006; Healy et al., 2010; Köllner et al., 2017; Shen et al., 2019)	Salt; Sulfate; Nitrate	3300	8.8
Sum				37,406	100

2024b). The original 1D MS patterns with mass-to-charge ratios (m/z) ranging from −120 to +120 excluding 0 are transformed into 2D representations, i.e., the original MS vector $X = [x_1, \ldots, x_{240}]$ is converted into a matrix whose product of rows (m) and columns (n) is 240. It was experimentally confirmed that the best performance is acquired when the MS patterns are transformed into a matrix of dimension $m \times n = 16 \times 15$ as input to the 2D-CNN model.

For training and testing, the benchmark dataset described in Section 4.1 was randomly split into two parts: 80 % (29,924 samples) for training and validation, and 20 % (7482 samples) for final testing, with equal class distribution in both parts. To address class imbalance, we applied random over-sampling for minority classes and under-sampling for majority classes during training. Additionally, to reduce the impact of random sampling on training reliability 5-fold cross-validation was applied, with each fold subsequently serving as validation while the remaining were used for training. The final model performance was evaluated on the independent test set.

The 2D-CNN architecture was optimized through grid search strategy, considering factors like the number and size of convolutional and pooling layers, kernel sizes, and fully connected (FC) layer structures. Fig. 6 shows the top-performing architecture, with four convolutional layers for MS pattern feature extraction. To preserve spatial dimensions, padding was applied ensuring that deeper layers receive sufficient information. After the fourth convolutional layer, a 3 × 3 max pooling layer down-sampled the features, reducing dimensionality and enhancing feature abstraction and robustness. Finally, two FC layers were used for classification. As output, each MS is attributed to one of the (here: 13) predefined classes, according to the highest probability of membership.

We used cross-entropy function to measure the inconsistency between predicted and true values during training and updated the network parameters with the Adam optimizer to minimize the loss function. The learning rate controls the step size of parameter update: a high rate may cause oscillation around the optimal solution, while a low rate ensures convergence but slows training and risks getting stuck in local optima. To balance efficiency and convergence, we applied a learning rate decay, starting at 0.0001 and reducing by 10 % every 100 epochs, for a total of 300 epochs. Additionally, batch normalization and dropout techniques were implemented to accelerate training and prevent overfitting (Wang et al., 2024b).

The experiments were performed with the following configurations: Windows 10, NVIDIA GeForce RTX 3090 graphics card, 3.2 GHz Intel Core i9-12900K processor and 64 GB DDR3 RAM. We used Python 3.10 and a machine learning framework PyTorch 1.12 to train the models. All libraries used in this work are open-source and cost-free.

Table 2 presents the prediction results of different models on the same test set (7482 samples), evaluated using the performance metrics accuracy, recall, precision, and F1 score. The last column in Table 2 lists the number of trainable parameters for each model. Due to the relatively small size of the 2D patterns in this study (16 × 15), classical CNN algorithms designed for image classification like AlexNet (Krizhevsky et al., 2017) and VGG (Simonyan and Zisserman, 2015) underperform because their larger convolutional kernels and deeper networks are not suited for the classification of SPMS data. For example, AlexNet's first convolutional kernel is 11 × 11, and even the smallest VGG architecture, VGG11, has eight layers. To adapt AlexNet and VGG to process SPMS data, we adjusted parameters, including the size of each convolutional layers and first FC layer, greatly reducing the number of parameters.

The results in Table 2 show that using 2D representations of MS patterns followed by 2D-CNN classification outperforms all other tested algorithms, even the 1D-CNN approach (Wang et al., 2023) designed to directly processes the original 1D MS patterns. Moreover, this is achieved with the smallest number of parameters among the models. Whereas the average training time for 2D-CNN was approx. 1 h, the time needed to test the network is seconds.

The confusion matrix in Fig. 7 documents the accuracy of the 2D-CNN model when classifying the 7482 samples from the test set into one of the 13 predefined classes. The main diagonal displays the rate of correct classifications for each class (true positive (TP) rates). The average accuracy over all classes is 92.0 %. Eight classes show accuracies of >90 % (of which three classes exceed 95 %). The remaining five classes are the V-rich class (87.6 %) and four classes of iron-containing particles (Fe-Sul-Nit, Fe-Nit, Fe-Nit-EC, Fe-dominant (85.3 %–89.8 %).

All entries other than on the confusion matrix' diagonal express

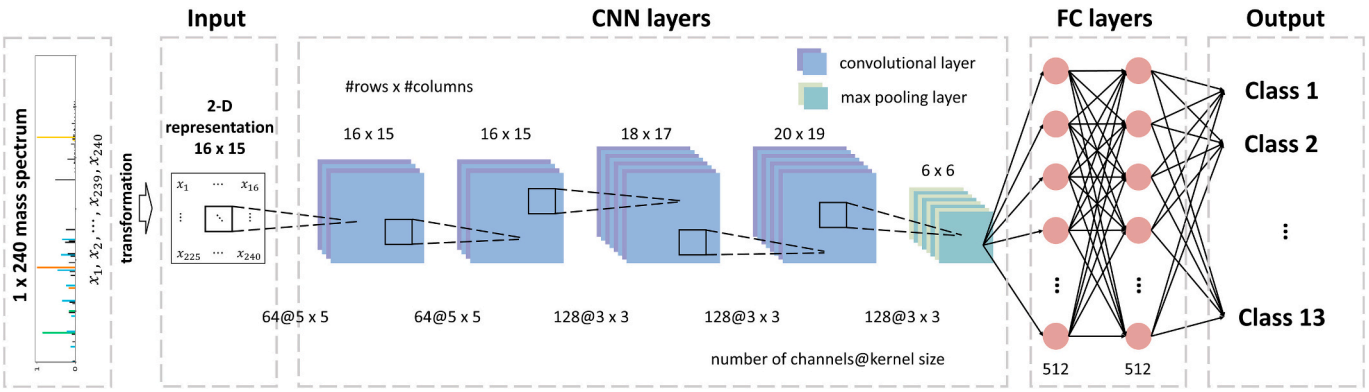

Fig. 6. Architecture of the 2D-CNN for the classification of mass spectral patterns of aerosol particles (Wang et al., 2024b).

incorrect classifications, with the entries in rows ('true labels') being class-specific false negative (FN) rates (i.e. wrongly dismissed assignments to that class) and the entries in columns ('predicted labels') being false positive (FP) rates (i.e. wrong assignments to that class). For the V-rich class, $FN_{V\text{-}rich}$ (5th row) is generally higher than $FP_{V\text{-}rich}$ (5th column), meaning that particles from other classes are rarely misidentified as V-rich particles, but a larger number of V-rich particles are misclassified as belonging to other. As an effect, if V-rich particles are identified, they are likely stemming from HFO combustion (precision $= \frac{TP_{V-rich}}{TP_{V-rich}+FP_{V-rich}} = 93.2$ %), but a number of V-rich particles may be overlooked (false missing rate $= \frac{FN_{V-rich}}{FN_{V-rich}+TP_{V-rich}} = 11.9$ %).

By examining the misclassified particles, we found that many false positive classifications ('predicted label') of spectra labeled as belonging to the V-rich class ('true label') are due to the bias introduced by our labeling rules. As described above, spectra with weak ion peak intensities of the combination of $^{51}V^{+}/^{67}[VO]^{+}$, $^{58/60}Ni^{+}$, and $^{54/56}Fe^{+}$ ions were labeled as V-rich in the benchmark dataset, even when peaks of other ions were dominant. This rule was applied for labeling V-rich particles to enable the model to be sensitive to the V-rich particles from HFO combustion. Another reason for V-rich misclassifications is that our dataset has a class imbalance problem. In future work, data augmentation methods shall be applied (Wang et al., 2024c) which help to increase the number of samples from certain classes (e.g., V-rich class) and to reduce class imbalances.

Spectra of iron-containing particles (mostly from emissions from MGO combustion) were classified into five subclasses, which represent different 'ages' of analyzed particles due to different distances from the emission source. As can be seen in Fig. 8, the main influences of aging effects on the MS are in the anions' spectra. The freshly emitted particles typical show strong EC signals (class 'Fe-EC'). As particles are transported by air, the EC peaks become progressively weaker, in contrast to peaks from nitrate ions, which are enhanced (classes 'Fe-Sul-Nit', 'Fe-Nit-EC', 'Fe-Nit') (Passig et al., 2022). The differences between these spectra are, however, comparatively small, making it difficult even for experts to set rules or thresholds to reliably distinguish between them. Hence, it is no surprise that – as the confusion matrix shows – most of misclassified spectra of iron-containing particles are assigned to one of the other subclasses. However, misclassifications into the iron-specific subclasses do not affect the identification of ships using HFO.

Table 2
Classification results in % of different algorithms on the test set (~7500 samples) with 5-fold cross-validation.

Algorithm	Accuracy	Recall	Precision	F1 score	No. of Parameters
AlexNet (Krizhevsky et al., 2017)	87.5 ± 0.5	87.4 ± 0.6	87.1 ± 0.4	87.2 ± 0.5	57.0 M
VGG11 (Simonyan and Zisserman, 2015)	89.5 ± 0.3	89.4 ± 0.3	89.4 ± 0.1	89.3 ± 0.3	30.2 M
1D-CNN (Wang et al., 2023)	90.4 ± 0.9	89.2 ± 0.2	90.1 ± 0.2	89.6 ± 0.3	30.6 M
2D-CNN (Wang et al., 2024b)	92.0 ± 0.1	91.9 ± 0.1	91.9 ± 0.1	91.9 ± 0.1	2.7 M

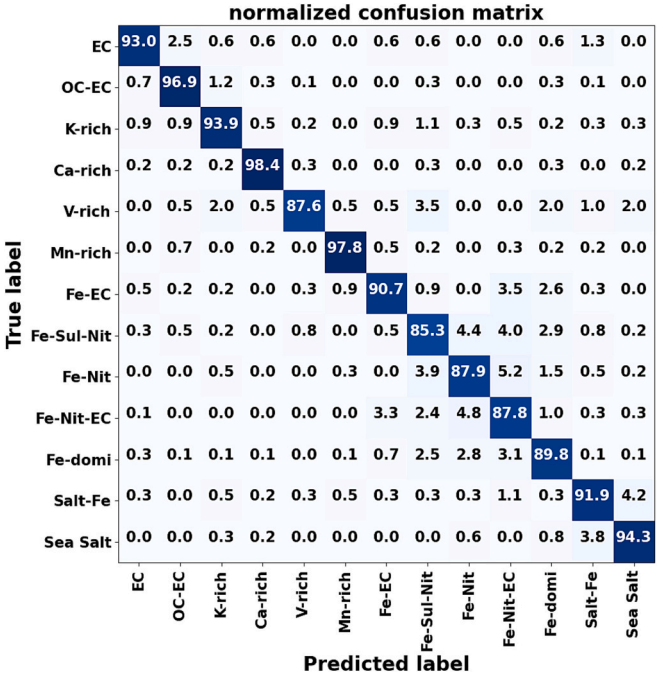

Fig. 7. Normalized confusion matrix illustrating the results of classification in % on the test set (~7500 samples) using the trained 2D-CNN model. The vertical axis shows the ground truth, and the horizontal axis displays the predictions. The main diagonal displays the rate of correct classifications for each of the 13 predefined classes. All other entries areas in the matrix express incorrect classifications, with the entries in rows being false negative (false missing) rates and the entries in columns being false positive (false alarm) rates.

5.2. Ship detection

To confirm whether a ship entering or leaving Rostock harbor was operating on HFO fuel, a 3-step-procedure was implemented. Ground are the classes as predicted by the 2D-CNN model of the MS pattern of all detected aerosol particles. These classes represent several probable sources of emission. As stated earlier, ships running on HFO will likely release a significant number of V-rich particles (Ault et al., 2009; Passig et al., 2022, 2021; Toner et al., 2006). The following steps are taken to

localize the emission source, if a particle is predicted to be of the V-rich class: First, the time stamp will be tagged when the concentration of V-rich particles in the 2D-CNN model's prediction is above a reasonable threshold of 1 % of all particles detected in a 10-minute-interval. Second, the meteorological data at the marked time are considered, specifically the reported wind direction and speed, in order to estimate the location of the emission plume identified as releasing V-rich particles. The last step is to search in the AIS database whether a ship passage event has occurred at the specific time and location when significant V-rich particle emissions could be traced back. In this study, only large ships with a minimum length of 75 m were considered as potential targets, and smaller ships in the AIS database were ignored.

We completed a comprehensive analysis of all spectra measured by the SPMS instrument during seven consecutive days from July 12th 2022, 00:00:00 to July 18th 2022, 23:59:59 (HH:MM:SS). Of course, none of the SPMS spectra recorded during that period were included in the benchmark dataset used for training and test, so that the seven-day predictions were completely independent.

Fig. 9 shows the analysis for one day (July 17th 2022) and serves as an example to discuss the results. The horizontal axis of each subplot has the timescale 00:00:00 to 23:59:59 with 10-minute intervals. In Fig. 9(a) and (b) the predictions over time of the 2D-CNN model of class distributions are given in absolute (a) and relative (b) numbers of particles in one of the 13 classes, integrated in intervals of 10 min and shown in color-coded bars of 10-minute width. The meaning of the colors is displayed on the right-hand site of graphs (a) and (b). Fig. 9(c) visualizes the mean wind direction and wind speed in 10-minute-intervals, as reported from the local DWD meteorological station. The arrow's angle represents the wind direction and the arrow's length indicates the speed. The scales of both measures are shown in the legend on the right. The

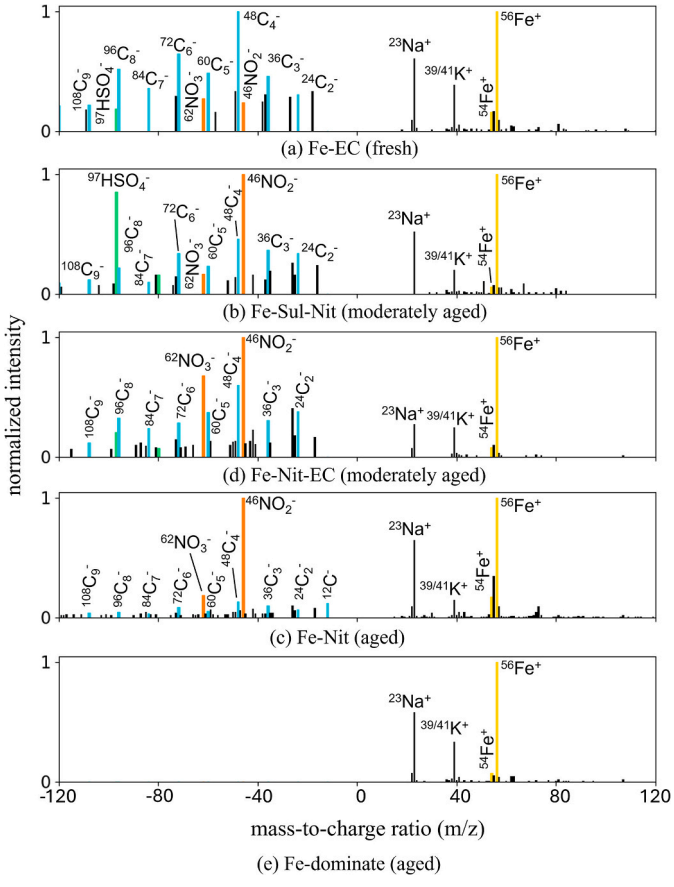

Fig. 8. Exemplary mass spectral patterns of iron-containing subclasses of aerosol particles.

displayed wind data help to roughly estimate where the particles have been transported from. The left vertical axis in Fig. 9(d) is the percentage of V-rich particles within a 10-minute interval, extracted from Fig. 9(b). If the percentage of V-rich particles is equal to or >1 % the bars are colored yellow, and green otherwise.

To verify the performance of the trained CNN model, we manually checked all 355 MS patterns predicted as belonging to the V-rich class on that day. Of these 355 predictions, 15 predictions could not be confirmed (true positive rate of 95.8 %). We then manually checked the prediction results for all particles from 00:00:00 to 12:00:00 on the same day (18,452 MS patterns) to reveal the number and time instants of V-rich particles that were not identified by the CNN model. We found only ~70 particles that were not but should be attributed to the V-rich class (false missing rate ~0.4 %). Most of these misclassified particles showed a mixed state with marker ions from other classes, i.e. their MS patterns contained not only the ion markers of the V-rich class, but also of other classes, and the intensities of $^{51}V^{+}/^{67}[VO]^{+}$, $^{58/60}Ni^{+}$, and $^{54/56}Fe^{+}$ ions were weak. Since the number of unidentified V-rich particles is small, the effect on the identification of ships running on HFO is negligible. We found, that the ship type (passenger ship, cargo ship or tanker) had no effect on the quality of CNN's predictions.

Also in Fig. 9(d), passing events of ships are marked in different colors, whether they enter (red markers) or leave (blue markers) the harbor area, according to the positions recorded in the AIS data logger. The length of these markers is 10 min, as is the average passing time through the predefined Search Area. On the right vertical axis of Fig. 9 (d), 10 individual ships are displayed, for which an emission plume containing particles in the V-rich class was predicted by the 2D-CNN model on that day. Of these 10 ships, in total 30 passages were recorded in the AIS database on that day. SHIP5, SHIP9, and SHIP10 entered the harbor and did not leave it that day, while the remaining seven ships (mostly ferries) passed the sampling site at least twice, up to eight times that day. (According to the AIS database, six more individual large ships passed through the Search Area on that day. However, no V-rich particles were detected at the time of their presence in the Search Area, and therefore their passages are not shown in Fig. 9(d)). Dash-lined squares around the markers in Fig. 9(d) indicate passage events that were identified as ships running on HFO, due to the V-rich content of the emission plume >1 % along with supporting indications from wind and AIS data. Of the 30 passages noted as likely emission events from HFO combustion, 21 passages (70 %) were identified, from all 10 targeted ships. Unfortunately, we could neither conduct an on-board check nor had we access to filed information what type of fuel a ship actually was using.

Let us discuss now on behalf of one example, how these target emissions were confirmed based on the automated CNN's predictions and the supporting wind and AIS data. As can be seen in Fig. 9(d), during the interval from 00:10:00 to 00:20:00, 1.9 % of all particles recorded in that period were predicted as V-rich, what is displayed by a yellow bar. Since this concentration is above the preset threshold of 1 %, this significant appearance V-rich particles is considered likely stemming from a ship in the Search Area running on HFO. At the time of passage, the wind direction was 300 degree (north-west) and the wind speed was 9.8 m/s (which is considered strong, but not too strong wind for a plume to be quickly dispersed). From these wind data it could be estimated that the emission source of that particle plume was approx. 750 m away from the sampling site in north-western direction, which is roughly in the center of the Search Area. At the time of detection, the AIS database lists SHIP1 on its way out of the harbor area, passing the assumed emission source location at 00:06:38. Adding the travel time (~75 s) of the particles to the sampling site means that the plume should be observable at around 00:08:00 in the SPMS results. According to the CNN's predictions, significant V-rich particle concentrations appear in the interval from 00:10:00 to 00:20:00, see the first yellow bar in Fig. 9(d), which – considering our rough estimations – is counted as confirmation that SHIP1 was running on HFO that night. (Perhaps the wind conditions on

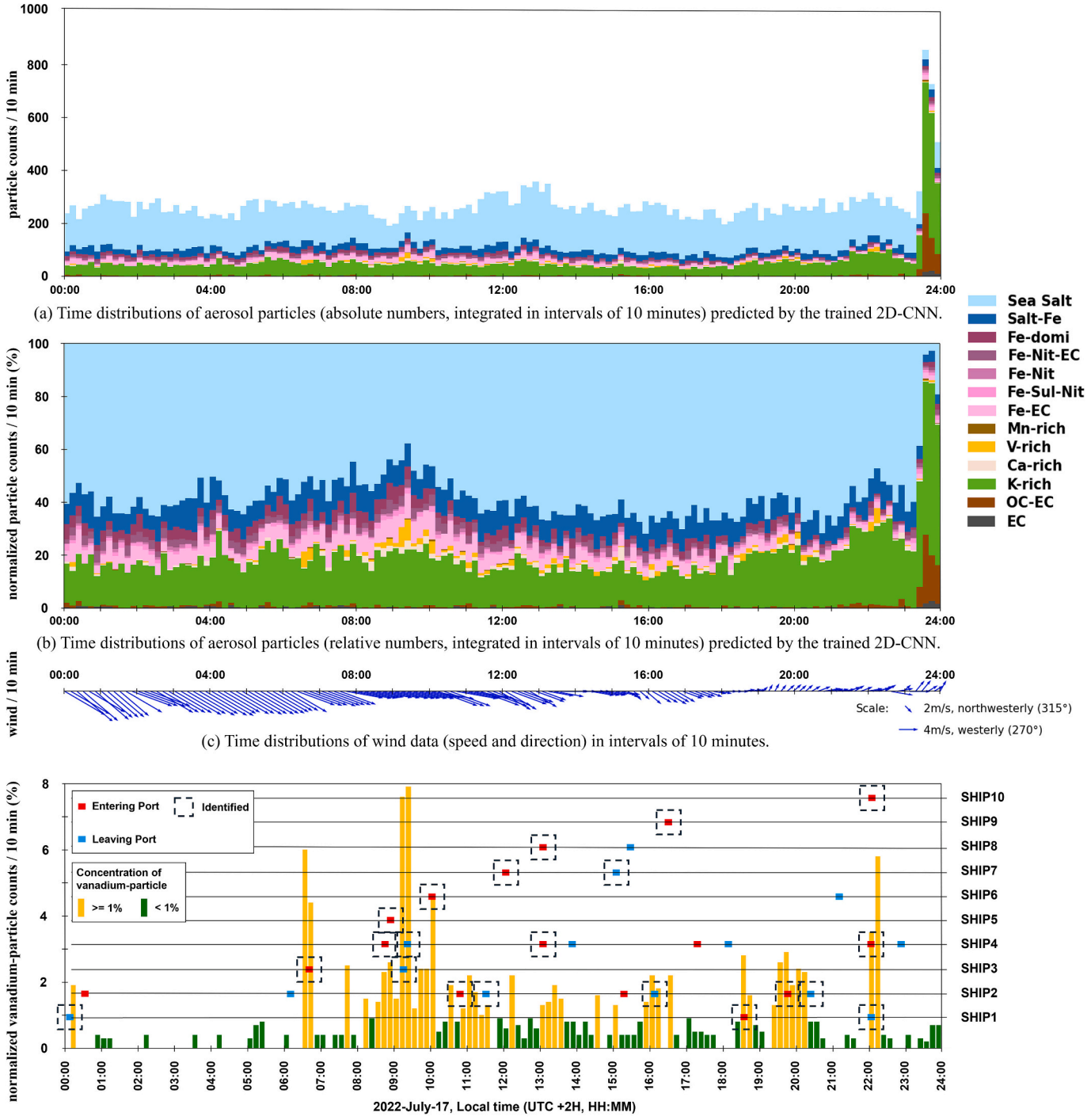

(a) Time distributions of aerosol particles (absolute numbers, integrated in intervals of 10 minutes) predicted by the trained 2D-CNN.

(b) Time distributions of aerosol particles (relative numbers, integrated in intervals of 10 minutes) predicted by the trained 2D-CNN.

(c) Time distributions of wind data (speed and direction) in intervals of 10 minutes.

(d) Time distributions of predicted vanadium-containing aerosol particles and the detection results of ship using HFO.

Fig. 9. Time distributions of aerosol particle classes predicted by the trained 2D-CNN model for 24 h of measurements (July 17th 2022), with (a) absolute and (b) relative numbers of particles per class, integrated in intervals of 10 min. The names and colors of each of the 13 regarded particle classes are shown in the legend on the right. In (c), wind speed and direction are displayed in intervals of 10 min, with scales of speed and direction (angle) given on the right. In (d), the left vertical axis gives the particle number concentration (in %) of V-rich class particles over a 10-minute interval, shown in two colors according to a threshold of 1 % of all particles in the time interval. The red and blue markers represent the time of passages of all 10 ships detected as potentially using polluting HFO, when they enter or leave the Search Area, respectively, according to the AIS database. Dash-lined squares around these markers indicate passages of ships using HFO detected by associating the V-ion predictions with wind measurements and AIS data at the same time.

the particles' path from the traveling ship to the sampling site were slightly different from the recordings of the DWD meteorological station some 2 km away.)

The next instance of V-rich particles in the measured aerosols is predicted at around 00:50:00, see the first green bar in Fig. 9(d). The concentration, however, is below 0.5 %. At the time of observation (minus travel time of the particles) no ship (even a smaller one) was listed in the AIS database. We assume that these V-rich particles (and others observed that night) come from ships outside of the Search Area. By reviewing the MS patterns, we found that these particles are

generally highly aged (i.e. they contain stronger nitrate signals or almost no contributions in anions' MS), being transported over a longer distance.

Table 3 records the results of the detected passages per day of the observation period, as found following the described procedure. In total, the AIS data recorded a total of 310 passing events of 57 different large ships (with lengths of >75 m) sailing into or out of the harbor during the seven days of observation. Matching the CNN's predictions with the wind and AIS data, 80 passages of 21 different ships were identified as sources of emission of the detected V-rich particles. Counting the passages on a day-by-day basis, the overall number of passages from these 21 ships was 180, of which as much as 80 passages (44.4 %) were automatically identified by our analysis. The remaining 36 ships (including some ferries) could not be detected every day they showed up at Rostock harbor.

The results in Table 3 show that the detection rates varied across different days, despite the relatively stable ship traffic in the Search Area, which averaged around 40 to 50 passages per day, as indicated by the AIS data. It must be underlined, that the detection results are highly dependent not only on the wind conditions (directions and speed), but also on humidity of the local air, as the meteorological conditions affect the number of collectable particles from the air (Celik et al., 2020; Passig and Zimmermann, 2021). Rainfall on July 14th and July 15th and high wind speeds during July 15th and July 16th were clearly not favorable for the collection of particles.

Table 4 shows the types of the detected 21 ships, the total number of times they passed through the Search Area during the seven days of observation, the number of times they were detected as potentially using HFO, and the rate of detection. The ships from SHIP1 to SHIP10 are the same ships as marked in Fig. 9(d). The results show that the emission of V-rich particles was identified in 7 out of 8 times (87.5 %), when SHIP1 (a ferry) passed the sampling site. SHIP9, SHIP11, and SHIP18 were detected during each individual passage (100 %)! (SHIP9 and SHIP11 passed twice and four times, SHIP18 only once during that week.)

The total number of passages of these 21 ships identified as running on HFO at least once during the seven days was 217, according to the AIS data. The difference to the 180 passages of these 21 ships when counted on a day-by-day basis (Table 3) can be easily explained: For example, SHIP5 was identified as running on HFO during its single passage on July 17th. According to the AIS data, SHIP5 passed through the Search Area two more times during those seven days of observation, on July 12th and 18th. Significant emissions of V-rich particles, however, were not detected during these two passages. This is probably due to either the usage of a fuel type not containing V^+ ions (e.g. MGO) or unfavorable wind directions. Thus, counting passages of ships identified as running on HFO on a day-by-day basis (Table 3), from the three passages of SHIP5 during the seven days of observation only the passage on July 17th was detectable and considered when calculating the detection rate.

Moreover, calculating the detection rates in Table 4 for all ships identified as using HFO fuel at least once, we assumed that individual ships run on the same fuel in all passages. In practice, there are 'hybrid' ships using different types of fuel or switching to battery-powered electric engines when entering and leaving a port. For example, SHIP4, SHIP6, and SHIP8 were more frequently detected when entering the harbor, but not when leaving. If the switching between engines and the usage of different fuels were recorded and known, our detection rates could be dramatically increased.

Another interesting event, recorded on July 17th by the measurement system and predicted by the CNN model, but not related to ship traffic, occurred after 23:00:00 and lasted until July 18th. As can be seen in Fig. 9(a) and (b), a large number of particles was recorded. As became apparent later and was even published in the local press, the reason for that tremendous increase of particles from biomass burning (mainly classified as EC-OC and K-rich) was the outbreak of a large fire ~5 km away from the sampling site. This observation once again underscores the capability of the SPMS system to monitor the air quality in a larger region and to reliably classify probable emission sources through our deep learning prediction model.

6. Conclusion and outlook

This study demonstrates for the first time the potential of combining sensitive and specific single-particle mass spectrometry (SPMS) with deep learning for real-time identification of relevant emissions through the classification of aerosol particles. On behalf of an advanced automated feature extraction based on an optimized 2D convolutional neural network (2D-CNN), the system proved to be a valuable tool for

Table 4
Detection results for each of the 21 ships identified as using HFO at least once.

Detected ship	Type of ship	Length in m	No. of passages	No. of detected passages	Detection rate (%)
SHIP1	Passenger	179	8	7	87.5
SHIP2	Passenger	170	59	18	30.5
SHIP3	Passenger	229	6	4	66.7
SHIP4	Passenger	170	68	20	29.4
SHIP5	Tanker	144	3	1	33.3
SHIP6	Cargo	154	2	1	50.0
SHIP7	Passenger	177	10	4	40.0
SHIP8	Passenger	200	22	4	18.2
SHIP9	Cargo	83	2	2	100.0
SHIP10	Passenger	150	2	1	50.0
SHIP11	Passenger	191	4	4	100.0
SHIP12	Cargo	122	2	1	50.0
SHIP13	Cargo	174	6	2	33.3
SHIP14	Cargo	187	4	3	75.0
SHIP15	Cargo	218	4	2	50.0
SHIP16	Cargo	82	3	1	33.3
SHIP17	Cargo	90	2	1	50.0
SHIP18	Cargo	193	1	1	100.0
SHIP19	Passenger	299	2	1	50.0
SHIP20	Cargo	229	5	1	20.0
SHIP21	Cargo	166	2	1	50.0
Sum			217	80	36.9

Table 3
Local wind conditions, total number of large ships (>75 m) passing through the search area and number of passages where HFO usage was detected on each of seven consecutive days.

	July 12	July 13	July 14	July 15	July 16	July 17	July 18	Sum
Local wind directions (N-north, *E*-east, S-south, W-west)	NW-W-SW	SW-W-NW	NW-W-NW	NW-SW	SW-NW	NW-SW	SW-S	–
Local wind speed (m/s)	4.9 ± 1.3	5.4 ± 3.1	8.7 ± 2.5	9.9 ± 2.7	10.3 ± 3.1	6.2 ± 2.8	2.7 ± 0.8	–
Rainfall (yes/no)	No	No	Yes	Yes	No	No	No	–
No. of large ships (from AIS)	20	22	20	18	15	16	17	In total: 57 ships
No. of passages (from AIS)	43	48	51	43	42	39	44	310
No. of detected ships using HFO fuels	6	9	6	5	4	10	6	In total: 21 ships
No. of passages of detected ships (from AIS) (A)	25	27	27	22	23	30	26	180 (from 21 ships)
No. of detected passages (B)	11	17	9	6	5	21	11	80 (from 21 ships)
Detection rate (B/A) (%)	44.0	63.0	33.3	27.3	21.7	70.0	42.3	44.4

identifying emission plumes of ships in coastal areas, stemming from the combustion of polluting fuels such as heavy fuel oil (HFO). Trained and validated with measurement data from a month-long campaign in the harbor area of Rostock, Germany, over 92 % accuracy was achieved in identifying 13 distinct classes of abundant aerosol particles. For the classification of V-rich particles the accuracy was 87.6 %, which can be explained by class imbalance of the created benchmark dataset and by the labeling rules assigning many particles as belonging to the V-rich class which are in fact in a mixed state.

By integrating predictions from 2D-CNN with meteorological data from a local weather station and ship positions from the Automatic Identification System (AIS), the system could identify a large number of ships running on HFO. For a period of seven consecutive days in July 2022, of 57 individual large ships entering or leaving the harbor area, 21 could be identified as using HFO at least once. The detection rate varied from day to day, depending on the number of particles from ship engine emissions detectable in the air, which are significantly affected by the wind direction and speed and the local meteorological conditions in general.

In addition, we understand the importance of the verification of ships which actually use HFO to raise the credibility. We approached the Federal Maritime and Hydrographic Agency (BSH) being the general public institution for maritime tasks in Germany, but could not get access to information about the detailed usage of fuels. To get such valuable information remains a task for the future.

Of note, the abundance of aerosol particles in the air is generally influenced by meteorological conditions (wind, rainfall, etc.) (Celik et al., 2020; Dall'Osto and Harrison, 2006; Passig and Zimmermann, 2021). The wind data used in this study were recorded by a German Weather Service (DWD) station located approximately 2 km north-west of the sampling site. In future measurement campaigns, we shall equip our mobile measurement system with appropriate weather sensors to measure the wind directly at the particle inlet. In this study we monitored ships at the port entry during westerly (northwest, west, southwest) wind. Establishing a system consisting of multiple linked SPMS devices around the monitoring area, this clear limitation could be eased.

Future research will also focus on identifying ships using MGO fuels by considering multiple iron-containing particle classes characteristic for ship emission plumes. The results in Fig. 9(b) show that using the iron-containing particles alone is not sufficient to identify ships using MGO, since iron-containing particles were abundant throughout the entire time of investigation and no distinct changes among the distribution of these classes could be observed. To achieve MGO identification, larger molecules with higher mass-to-charge ratios ($m/z > 140$) like polycyclic aromatic hydrocarbons should be also considered (Anders et al., 2024).

The success of the proposed flexible and real-time classification based on mass spectra of individual aerosol particles underscores its potential for broader application in air quality monitoring and environmental regulation. This work is a first step towards on-line classification of aerosol particles in maritime environments in order to remotely monitor and localize ship emissions from larger distances using meteorological and AIS position data, with the perspective of classifying both MGO and HFO fuels used by ships. Moreover, fully automated classification of particles enables the monitoring of a wider range of indicators (e.g., toxins, industrial emissions, chemical spills, fires, etc.), thus allows SPMS to support applications in broader areas such as hazard and air quality monitoring.

CRediT authorship contribution statement

Guanzhong Wang: Writing – original draft, Visualization, Validation, Software, Methodology, Formal analysis, Data curation, Conceptualization. **Heinrich Ruser:** Writing – review & editing, Validation, Methodology, Formal analysis, Conceptualization. **Julian Schade:** Writing – review & editing, Validation, Investigation. **Seongho Jeong:** Writing – review & editing, Validation, Investigation. **Johannes Passig:** Writing – review & editing, Validation, Investigation. **Ralf Zimmermann:** Writing – review & editing, Supervision. **Günther Dollinger:** Writing – review & editing, Supervision. **Thomas Adam:** Writing – review & editing, Supervision, Project administration, Funding acquisition.

Declaration of competing interest

The authors declare that they have no known competing financial interests or personal relationships that could have appeared to influence the work reported in this paper.

Acknowledgements

This research is funded by dtec.bw – Digitalization and Technology Research Center of the Bundeswehr (project "LUKAS"). dtec.bw is funded by the European Union – NextGenerationEU. Contributions were also provided by the German Research Foundation (DFG), SFB 1477 "Light-Matter Interactions at Interfaces", project number 441234705.

Data availability

Data will be made available on request.

References

Abdul Jameel, A.G., Alkhateeb, A., Telalović, S., Elbaz, A.M., Roberts, W.L., Sarathy, S. M., 2019. Environmental challenges and opportunities in marine engine heavy fuel oil combustion. In: Murali, K., Sriram, V., Samad, A., Saha, N. (Eds.), Proceedings of the Fourth International Conference in Ocean Engineering (ICOE2018). Springer, Singapore, pp. 1047–1055. https://doi.org/10.1007/978-981-13-3119-0_72.

Alzubaidi, L., Zhang, J., Humaidi, A.J., Al-Dujaili, A., Duan, Y., Al-Shamma, O., Santamaría, J., Fadhel, M.A., Al-Amidie, M., Farhan, L., 2021. Review of deep learning: concepts, CNN architectures, challenges, applications, future directions. J. Big Data 8, 53. https://doi.org/10.1186/s40537-021-00444-8.

Anders, L., Schade, J., Rosewig, E.I., Schmidt, M., Irsig, R., Jeong, S., Käfer, U., Gröger, T., Bendl, J., Saraji-Bozorgzad, M.R., Adam, T., Etzien, U., Czech, H., Buchholz, B., Streibel, T., Passig, J., Zimmermann, R., 2024. Polycyclic aromatic hydrocarbons as fuel-dependent markers in ship engine emissions using single-particle mass spectrometry. Environ. Sci. Atmos. 4, 708–717. https://doi.org/10.1039/D4EA00035H.

Arndt, J., Healy, R.M., Setyan, A., Flament, P., Deboudt, K., Riffault, V., Alleman, L.Y., Mbengue, S., Wenger, J.C., 2021. Characterization and source apportionment of single particles from metalworking activities. Environ. Pollut. 270, 116078. https://doi.org/10.1016/j.envpol.2020.116078.

Ault, A.P., Moore, M.J., Furutani, H., Prather, K.A., 2009. Impact of emissions from the Los Angeles Port Region on San Diego air quality during regional transport events. Environ. Sci. Technol. 43, 3500–3506. https://doi.org/10.1021/es8018918.

Beck, A.G., Muhoberac, M., Randolph, C.E., Beveridge, C.H., Wijewardhane, P.R., Kenttämaa, H.I., Chopra, G., 2024. Recent developments in machine learning for mass spectrometry. ACS Meas. Sci. Au 4, 233–246. https://doi.org/10.1021/acsmeasuresciau.3c00060.

Beecken, J., Mellqvist, J., Salo, K., Ekholm, J., Jalkanen, J.-P., Johansson, L., Litvinenko, V., Volodin, K., Frank-Kamenetsky, D.A., 2015. Emission factors of SO_2, NO_x and particles from ships in Neva Bay from ground-based and helicopter-borne measurements and AIS-based modeling. Atmospheric Chemistry and Physics 15, 5229–5241. https://doi.org/10.5194/acp-15-5229-2015.

Blasco, J., Durán-Grados, V., Hampel, M., Moreno-Gutiérrez, J., 2014. Towards an integrated environmental risk assessment of emissions from ships' propulsion systems. Environ. Int. 66, 44–47. https://doi.org/10.1016/j.envint.2014.01.014.

Cariou, P., Guët, A.T., Monios, J., Halim, R.A., 2024. The economic impact of the Mediterranean Sulfur Emission Control Area. Mar. Policy 168, 106300. https://doi.org/10.1016/j.marpol.2024.106300.

Celik, S., Drewnick, F., Fachinger, F., Brooks, J., Darbyshire, E., Coe, H., Paris, J.-D., Eger, P.G., Schuladen, J., Tadic, I., Friedrich, N., Dienhart, D., Hottmann, B., Fischer, H., Crowley, J.N., Harder, H., Borrmann, S., 2020. Influence of vessel characteristics and atmospheric processes on the gas and particle phase of ship emission plumes: in situ measurements in the Mediterranean Sea and around the Arabian Peninsula. Atmos. Chem. Phys. 20, 4713–4734. https://doi.org/10.5194/acp-20-4713-2020.

Chen, D., Xiao, H.-Y., Sun, N., Yan, J., Yin, S., 2024. Characterizing leaf-deposited particles: single-particle mass spectral analysis and comparison with naturally fallen particles. Environ. Sci. Ecotechnol. 21, 100432. https://doi.org/10.1016/j.ese.2024.100432.

Christopoulos, C.D., Garimella, S., Zawadowicz, M.A., Möhler, O., Cziczo, D.J., 2018. A machine learning approach to aerosol classification for single-particle mass

spectrometry. Atmos. Meas. Tech. 11, 5687–5699. https://doi.org/10.5194/amt-11-5687-2018.
Dall'Osto, M., Harrison, R., 2006. Chemical characterisation of single airborne particles in Athens (Greece) by ATOFMS. Atmos. Environ. 40, 7614–7631. https://doi.org/10.1016/j.atmosenv.2006.06.053.
Dall'Osto, M., Harrison, R.M., 2012. Urban organic aerosols measured by single particle mass spectrometry in the megacity of London. Atmos. Chem. Phys. 12, 4127–4142. https://doi.org/10.5194/acp-12-4127-2012.
Dulebenets, M.A., 2016. Advantages and disadvantages from enforcing emission restrictions within emission control areas. Marit. Bus. Rev. 1, 107–132. https://doi.org/10.1108/MABR-05-2016-0011.
Eyring, V., Isaksen, I.S.A., Berntsen, T., Collins, W.J., Corbett, J.J., Endresen, O., Grainger, R.G., Moldanova, J., Schlager, H., Stevenson, D.S., 2010. Transport impacts on atmosphere and climate: shipping. Atmos. Environ. 44, 4735–4771. https://doi.org/10.1016/j.atmosenv.2009.04.059. Transport Impacts on Atmosphere and Climate: The ATTICA Assessment Report.
Fu, M., Ding, Y., Ge, Y., Yu, L., Yin, H., Ye, W., Liang, B., 2013. Real-world emissions of inland ships on the Grand Canal, China. Atmos. Environ. 81, 222–229. https://doi.org/10.1016/j.atmosenv.2013.08.046.
Fuglestvedt, J., Berntsen, T., Eyring, V., Isaksen, I., Lee, D.S., Sausen, R., 2009. Shipping emissions: from cooling to warming of climate—and reducing impacts on health. Environ. Sci. Technol. 43, 9057–9062. https://doi.org/10.1021/es901944r.
German Weather Service (DWD), 2022. Meteorological Data From German Weather Service Station 4271 [WWW Document]. URL. https://opendata.dwd.de/climate_environment/CDC/observations_germany/climate/10_minutes/wind/ (accessed 4.1.25).
Healy, R.M., O'Connor, I.P., Hellebust, S., Allanic, A., Sodeau, J.R., Wenger, J.C., 2009. Characterisation of single particles from in-port ship emissions. Atmos. Environ. 43, 6408–6414. https://doi.org/10.1016/j.atmosenv.2009.07.039.
Healy, R.M., Hellebust, S., Kourtchev, I., Allanic, A., O'Connor, I.P., Bell, J.M., Healy, D. A., Sodeau, J.R., Wenger, J.C., 2010. Source apportionment of PM2.5 in Cork Harbour, Ireland using a combination of single particle mass spectrometry and quantitative semi-continuous measurements. Atmos. Chem. Phys. 10, 9593–9613. https://doi.org/10.5194/acp-10-9593-2010.
Healy, R.M., Sciare, J., Poulain, L., Kamili, K., Merkel, M., Müller, T., Wiedensohler, A., Eckhardt, S., Stohl, A., Sarda-Estève, R., McGillicuddy, E., O'Connor, I.P., Sodeau, J. R., Wenger, J.C., 2012. Sources and mixing state of size-resolved elemental carbon particles in a European megacity: Paris. Atmos. Chem. Phys. 12, 1681–1700. https://doi.org/10.5194/acp-12-1681-2012.
Heikkilä, P., Rostedt, A., Toivonen, J., Keskinen, J., 2024. Analysis and classification of individual ambient aerosol particles with field-deployable laser-induced breakdown spectroscopy platform. Aerosol Sci. Technol. 58, 1063–1078. https://doi.org/10.1080/02786826.2024.2350022.
IMO, 2016. Sulphur oxides (SOx) – Regulation 14 [WWW Document]. URL. www.imo.org (accessed 4.1.25).
Jeong, S., Bendl, J., Saraji-Bozorgzad, M., Käfer, U., Etzien, U., Schade, J., Bauer, M., Jakobi, G., Orasche, J., Fisch, K., Cwierz, P.P., Rüger, C.P., Czech, H., Karg, E., Heyen, G., Krausnick, M., Geissler, A., Geipel, C., Streibel, T., Schnelle-Kreis, J., Sklorz, M., Schulz-Bull, D.E., Buchholz, B., Adam, T., Zimmermann, R., 2023. Aerosol emissions from a marine diesel engine running on different fuels and effects of exhaust gas cleaning measures. Environ. Pollut. 316, 120526. https://doi.org/10.1016/j.envpol.2022.120526.
Kattner, L., Mathieu-Üffing, B., Burrows, J.P., Richter, A., Schmolke, S., Seyler, A., Wittrock, F., 2015. Monitoring compliance with sulfur content regulations of shipping fuel by in situ measurements of ship emissions. Atmos. Chem. Phys. 15, 10087–10092. https://doi.org/10.5194/acp-15-10087-2015.
Köllner, F., Schneider, J., Willis, M.D., Klimach, T., Helleis, F., Bozem, H., Kunkel, D., Hoor, P., Burkart, J., Leaitch, W.R., Aliabadi, A.A., Abbatt, J.P.D., Herber, A.B., Borrmann, S., 2017. Particulate trimethylamine in the summertime Canadian high Arctic lower troposphere. Atmos. Chem. Phys. 17, 13747–13766. https://doi.org/10.5194/acp-17-13747-2017.
Krizhevsky, A., Sutskever, I., Hinton, G.E., 2017. Imagenet classification with deep convolutional neural networks. Commun. ACM 60, 84–90. https://doi.org/10.1145/3065386.
Lähteenmäki-Uutela, A., Yliskylä-Peuralahti, J., Repka, S., Mellqvist, J., 2019. What explains SECA compliance: rational calculation or moral judgment? WMU J. Marit. Aff. 18, 61–78. https://doi.org/10.1007/s13437-019-00163-1.
LeCun, Y., Bengio, Y., Hinton, G., 2015. Deep learning. Nature 521, 436–444. https://doi.org/10.1038/nature14539.
Mellqvist, J., Conde, V., Beecken, J., Ekholm, J., 2017. Certification of an Aircraft and Airborne Surveillance of Fuel Sulfur Content in Ships at the SECA Border. Chalmers University of Technology. https://doi.org/10.17196/COMPMON.002.
Moffet, R.C., de Foy, B., Molina, L.T., Molina, M.J., Prather, K.A., 2008. Measurement of ambient aerosols in northern Mexico City by single particle mass spectrometry. Atmos. Chem. Phys. https://doi.org/10.5194/acp-8-4499-2008.
Ni, P., Wang, X., Li, H., 2020. A review on regulations, current status, effects and reduction strategies of emissions for marine diesel engines. Fuel 279, 118477. https://doi.org/10.1016/j.fuel.2020.118477.
Passig, J., Zimmermann, R., 2021. Laser ionization in single-particle mass spectrometry. In: Zimmermann, R., Hanley, L. (Eds.), Photoionization and Photo-induced Processes in Mass Spectrometry. Wiley.
Passig, J., Schade, J., Irsig, R., Li, L., Li, X., Zhou, Z., Adam, T., Zimmermann, R., 2021. Detection of ship plumes from residual fuel operation in emission control areas using single-particle mass spectrometry. Atmos. Meas. Tech. 14, 4171–4185. https://doi.org/10.5194/amt-14-4171-2021.
Passig, J., Schade, J., Irsig, R., Kröger-Badge, T., Czech, H., Adam, T., Fallgren, H., Moldanova, J., Sklorz, M., Streibel, T., 2022. Single-particle characterization of polycyclic aromatic hydrocarbons in background air in northern Europe. Atmos. Chem. Phys. 22, 1495–1514. https://doi.org/10.5194/acp-22-1495-2022.
Pratt, K.A., Prather, K.A., 2012. Mass spectrometry of atmospheric aerosols—recent developments and applications. Part I: Off-line mass spectrometry techniques. Mass Spectrom. Rev. 31, 1–16.
Rosewig, E.I., Schade, J., Passig, J., Osterholz, H., Irsig, R., Smok, D., Gawlitta, N., Schnelle-Kreis, J., Hovorka, J., Schulz-Bull, D., Zimmermann, R., Adam, T.W., 2023. Remote detection of different marine fuels in exhaust plumes by onboard measurements in the Baltic Sea using single-particle mass spectrometry. Atmosphere 14, 849. https://doi.org/10.3390/atmos14050849.
Rosewig, E.I., Schade, J., Ruser, H., Passig, J., Zimmermann, R., Adam, T.W., 2024. Detection and analysis of ship emissions using single-particle mass spectrometry: a land-based field study in the port of Rostock, Germany. Atmos. Environ. X 24, 100302. https://doi.org/10.1016/j.aeaoa.2024.100302.
Schade, J., Passig, J., Irsig, R., Ehlert, S., Sklorz, M., Adam, T., Li, C., Rudich, Y., Zimmermann, R., 2019. Spatially shaped laser pulses for the simultaneous detection of polycyclic aromatic hydrocarbons as well as positive and negative inorganic ions in single particle mass spectrometry. Anal. Chem. 91, 10282–10288. https://doi.org/10.1021/acs.analchem.9b02477.
Shen, X., Saathoff, H., Huang, W., Mohr, C., Ramisetty, R., Leisner, T., 2019. Understanding atmospheric aerosol particles with improved particle identification and quantification by single-particle mass spectrometry. Atmos. Meas. Tech. 12, 2219–2240. https://doi.org/10.5194/amt-12-2219-2019.
Shen, X., Bell, D.M., Coe, H., Hiranuma, N., Mahrt, F., Marsden, N.A., Mohr, C., Murphy, D.M., Saathoff, H., Schneider, J., Wilson, J., Zawadowicz, M.A., Zelenyuk, A., DeMott, P.J., Möhler, O., Cziczo, D.J., 2024. Measurement report: the fifth international workshop on ice nucleation phase 1 (FIN-01): intercomparison of single-particle mass spectrometers. Atmos. Chem. Phys. 24, 10869–10891. https://doi.org/10.5194/acp-24-10869-2024.
Simonyan, K., Zisserman, A., 2015. Very Deep Convolutional Networks for Large-scale Image Recognition.
Su, B., Zhang, G., Song, C., Liang, Y., Wang, L., Li, L., Zhou, Z., Yan, J., Wang, X., Bi, X., 2024. Submicron organic aerosol types in the summertime Arctic: mixing state, geographic distribution, and drivers. J. Geophys. Res. Atmos. 129, e2024JD041061. https://doi.org/10.1029/2024JD041061.
Toner, S.M., Sodeman, D.A., Prather, K.A., 2006. Single particle characterization of ultrafine and accumulation mode particles from heavy duty diesel vehicles using aerosol time-of-flight mass spectrometry. Environ. Sci. Technol. 40, 3912–3921. https://doi.org/10.1021/es051455x.
Toscano, D., Murena, F., 2019. Atmospheric ship emissions in ports: a review. Correlation with data of ship traffic. Atmos. Environ. X 4, 100050. https://doi.org/10.1016/j.aeaoa.2019.100050.
UNCTAD, 2018. Review of Maritime Transport 2018. United Nations. https://doi.org/10.18356/cd4440fc-en.
UNCTAD, 2023. Review of Maritime Transport 2023: Towards a Green and Just Transition. United Nations. https://doi.org/10.18356/9789213584569.
Viana, M., Hammingh, P., Colette, A., Querol, X., Degraeuwe, B., Vlieger, I. de, van Aardenne, J., 2014. Impact of maritime transport emissions on coastal air quality in Europe. Atmos. Environ. 90, 96–105. https://doi.org/10.1016/j.atmosenv.2014.03.046.
Villa, T.F., Brown, R.A., Jayaratne, E.R., Gonzalez, L.F., Morawska, L., Ristovski, Z.D., 2019. Characterization of the particle emission from a ship operating at sea using an unmanned aerial vehicle. Atmos. Meas. Tech. 12, 691–702. https://doi.org/10.5194/amt-12-691-2019.
Wan, E., Zhang, Q., Li, L., Xie, Q., Li, X., Liu, Y., 2024. The online in situ detection of indoor air pollution via laser induced breakdown spectroscopy and single particle aerosol mass spectrometer technology. Opt. Lasers Eng. 174, 107974. https://doi.org/10.1016/j.optlaseng.2023.107974.
Wang, X., Shen, Y., Lin, Y., Pan, J., Zhang, Y., Louie, P.K.K., Li, M., Fu, Q., 2019. Atmospheric pollution from ships and its impact on local air quality at a port site in Shanghai. Atmos. Chem. Phys. 19, 6315–6330. https://doi.org/10.5194/acp-19-6315-2019.
Wang, G., Ruser, H., Schade, J., Passig, J., Adam, T., Dollinger, G., Zimmermann, R., 2023. 1D-CNN network based real-time aerosol particle classification with single-particle mass spectrometry. IEEE Sens. Lett. 7 (11), 1–4. https://doi.org/10.1109/LSENS.2023.3315554.
Wang, G., Ruser, H., Schade, J., Passig, J., Adam, T., Dollinger, G., Zimmermann, R., 2024a. Machine learning approaches for automatic classification of single-particle mass spectrometry data. Atmos. Meas. Tech. 17, 299–313. https://doi.org/10.5194/amt-17-299-2024.
Wang, G., Ruser, H., Schade, J., Passig, J., Zimmermann, R., Dollinger, G., Adam, T., 2024b. CNN-based aerosol particle classification using 2D representations of single-particle mass spectrometer data. In: 2024 International Conference on Artificial Intelligence in Information and Communication (ICAIIC), pp. 1–6. https://doi.org/10.1109/ICAIIC60209.2024.10463253. Presented at the 2024 International Conference on Artificial Intelligence in Information and Communication (ICAIIC).
Wang, G., Ruser, H., Schade, J., Passig, J., Zimmermann, R., Dollinger, G., Adam, T., 2024c. Rapid classification of aerosol particle mass spectra using data augmentation and deep learning. In: 2024 IEEE Conference on Artificial Intelligence (CAI), pp. 1167–1172. https://doi.org/10.1109/CAI59869.2024.00208. Presented at the 2024 IEEE Conference on Artificial Intelligence (CAI).
Xu, Y., Wang, Z., Pei, C., Wu, C., Huang, B., Cheng, C., Zhou, Z., Li, M., 2024. Single particle mass spectral signatures from on-road and non-road vehicle exhaust

particles and their application in refined source apportionment using deep learning. Sci. Total Environ. 930, 172822. https://doi.org/10.1016/j.scitotenv.2024.172822.
Ye, Y., Aizezi, N., Feng, J., Han, B., Li, X., Su, Z., Li, L., Liu, Y., 2025. Advanced characterization of industrial smoke: particle composition and size analysis with single particle aerosol mass spectrometry and optimized machine learning. Anal. Chem. 97, 5554–5562. https://doi.org/10.1021/acs.analchem.4c05988.
Yuan, H., Xiao, C., Wang, Y., Peng, X., Wen, Y., Li, Q., 2020. Maritime vessel emission monitoring by an UAV gas sensor system. Ocean Eng. 218, 108206. https://doi.org/10.1016/j.oceaneng.2020.108206.
Zhou, J., Wang, H., 2020. Study on efficient removal of SOx and NOx from marine exhaust gas by wet scrubbing method using urea peroxide solution. Chem. Eng. J. 390, 124567. https://doi.org/10.1016/j.cej.2020.124567.
Zhou, F., Fan, Y., Zou, J., An, B., 2022a. Ship emission monitoring sensor web for research and application. Ocean Eng. 249, 110980. https://doi.org/10.1016/j.oceaneng.2022.110980.
Zhou, L., Li, M., Cheng, C., Zhou, Z., Nian, H., Tang, R., Chan, C.K., 2022b. Real-time chemical characterization of single ambient particles at a port city in Chinese domestic emission control area — impacts of ship emissions on urban air quality. Sci. Total Environ. 819, 153117. https://doi.org/10.1016/j.scitotenv.2022.153117.
Zhu, M., Yuen, K.F., Ge, J.W., Li, K.X., 2018. Impact of maritime emissions trading system on fleet deployment and mitigation of CO2 emission. Transp. Res. Part D Transp. Environ. 62, 474–488. https://doi.org/10.1016/j.trd.2018.03.016.
Zis, T.P.V., Cullinane, K., Ricci, S., 2022. Economic and environmental impacts of scrubbers investments in shipping: a multi-sectoral analysis. Marit. Policy Manage. 49, 1097–1115. https://doi.org/10.1080/03088839.2021.1937742.